SAND2015-4109J

Random mask optimization for fast neutron coded aperture imaging

K. McMillan[a,b], P. Marleau[a], E. Brubaker[a]

[a]Sandia National Laboratories, 7011 East Ave, Livermore, CA 94550

[b]Now at University of California Los Angeles, 405 Hilgard Avenue, Los Angeles, CA 90095

Abstract

In coded aperture imaging, one of the most important factors determining the quality of reconstructed images is the choice of mask/aperture pattern. In many applications, uniformly redundant arrays (URAs) are widely accepted as the optimal mask pattern. Under ideal conditions, thin and highly opaque masks, URA patterns are mathematically constructed to provide artifact-free reconstruction however, the number of URAs for a chosen number of mask elements is limited and when highly penetrating particles such as fast neutrons and high-energy gamma-rays are being imaged, the optimum is seldom achieved. In this case more robust mask patterns that provide better reconstructed image quality may exist. Through the use of heuristic optimization methods and maximum likelihood expectation maximization (MLEM) image reconstruction, we show that for both point and extended neutron sources a random mask pattern can be optimized to provide better image quality than that of a URA.

1. Introduction

In coded aperture imaging, a mask array consisting of a pattern of transparent and opaque elements is placed in front of a position sensitive detection plane [1]. A radiation source located somewhere within the field of view of the imager casts a shadow of the mask plane onto the detection plane. One of the most important considerations in coded aperture imaging is the mask design. The attainable quality of the reconstructed images is strongly dependent upon the choice of aperture pattern. Optimally, mask patterns are designed such that the direction of the incident radiation is uniquely encoded in the pattern projected onto the detection plane. With suitable mask selection and reconstruction techniques, multiple sources and/or extended sources can be resolved since the projected shadow patterns in different directions are not only unique but also orthogonal.

A pinhole camera can be thought of as a special case of coded aperture imaging: it uses a mask that contains one central aperture in an array of otherwise opaque elements. While pinhole cameras are capable of high angular resolution, they tend to suffer from low efficiency due to the single small aperture. In coded aperture imaging the modulation detected at the image plane can

be thought of as the superposition of many pinhole camera images corresponding to the various apertures in the mask array [2]. Therefore, one major advantage of coded aperture imaging is that it provides a greater throughput of radiation while maintaining the same aperture size and thus angular resolution as a pinhole camera with the same aperture size.

An important design parameter of the mask array is the open fraction. The open fraction is defined as the ratio of the area of transparent elements of the mask (apertures) to the total area of transparent and opaque elements of the mask. There have been several approaches to calculating the optimal open fraction of a mask array [3,4]. Within these approaches, the optimal open fraction is a function of two characteristics of the imaging space: the fraction of the total source counts due to the source present as a function of reconstruction position, and the ratio of the counts at one reconstruction position due to un-modulated background to the total number of counts due to the source. The two source arrangements of interest in this work, a point source and an extended source, have distinct values of these characteristics and are therefore expected to have different optimal open fractions.

Over the last three or four decades, uniformly redundant arrays (URAs) and modified uniformly redundant arrays (MURAs) have been widely used and accepted as optimal mask patterns [5]. URAs and MURAs have different mathematical definitions, but very similar properties, and we will use URA to refer to both families hereafter. Under ideal conditions URA masks are mathematically guaranteed to provide artifact-free reconstruction from the modulation pattern observed on a position sensitive detector plane. However, these patterns exist only for a certain number of mask orders (number of elements in a pattern) and open fractions. In fact there are very few known URAs with open fraction significantly different from 50% [6]. Random masks are arrangements of transparent and opaque elements that are not constrained by any pre-defined pattern, although they may be optimized for performance, as will be shown in this work. In contrast with URA patterns, random masks can have any open fraction ranging from a single pinhole aperture to an inverse pinhole aperture with a single mask element.

In the past, motivation for using the URA mask stemmed from the fact that matched filtering could be employed to allow for the source distribution to be reconstructed from the coded projection by directly correlating it with the aperture array itself [2]. Because the URA autocorrelation function has constant sidelobes, i.e. positions misaligned with the true source direction sum to a constant value, matched filtering was ideal because the reconstruction was not subject to certain systematic errors that other, non-URA, arrays like random masks could display when this reconstruction technique was employed [5]. With wider use of iterative image reconstruction algorithms such as maximum likelihood expectation maximization (MLEM) and computer systems capable of handle their computationally intense nature, the need for matched filtering techniques is reduced [7].

Another important design parameter of the mask array is the mask order. The mask order is defined as the number of elements along each dimension of the smallest repeating unit of the

mask. The choice of mask order is typically dictated by constraints such as the size and resolution of the available detector and the desired size and resolution of the imaging space [5]. URAs exist only for mask array orders that are prime numbers. In order to have at least one full sample of the entire URA while maintaining a field of view larger than a single direction, either the detection plane must be larger than the URA pattern or the mask must consist of a tiling of a several URA units. While there is no limitation to the number of times the pattern can be repeated, frequently masks are constructed from a 2 x 2 tiling of the basic URA pattern with an additional dividing row and column included in order to avoid intrinsic ambiguities [1]. However, random masks can be built for any mask order, do not need to be fully sampled, and thus do not require a repeat of the pattern in order to increase the field of view.

Under ideal conditions, a URA mask provides perfect modulation and any backgrounds that may be present uniformly populate the detection plane. If these conditions are met, then the autocorrelation of the mask pattern is a delta function and the inherent symmetries associated with the tiling of the mask pattern for URAs perfectly cancel [5]. For x-ray detection, near ideal conditions can be satisfied with the use of thin, nearly perfectly opaque lead or tungsten mask elements resulting in relatively artifact-free reconstructions. However, for fast neutron detection, an equivalently opaque mask material does not exist. Low atomic number materials such as high-density polyethylene are the most attenuating to fast neutrons. In order to compensate for the highly penetrating neutrons, a mask made of high-density polyethylene must be made appreciably thick (several cm) in order to provide sufficient modulation.

As the mask thickness becomes appreciable compared to the size of the mask elements, the apertures become obscured at off-axis angles. This can result in the emergence of systematic noise in the sidelobes of the autocorrelation function [8] therefore tiled URA mask patterns may not necessarily be the optimal solution for fast neutron coded aperture imaging.

Using image reconstruction techniques other than match filtering (such as MLEM), random mask patterns can be optimized for open fractions that are specific to the characteristics of the source distribution under consideration. Considering an image quality figure of merit (FOM) that takes into account the differences between the true source distribution and the reconstructed source distribution, optimization is performed by employing a hybrid method combining elements of simulated annealing (SA) and the great deluge algorithm (GDA) [9]. In this work we show that this method is capable of generating random mask aperture patterns that converge to an open fraction that is optimal for any desired source distribution and an image quality better than URA masks.

Finally, we optimize and physically construct a random mask pattern for a selected source distribution. A series of measurements are made using the optimized mask and a URA mask with the same coded aperture detector system. Extended source distributions are simulated through the use of ^{252}Cf test sources moved through a pattern.

2. Materials and methods

2.1. Mask arrays

Three types of mask arrays are simulated and analyzed in this investigation: a single aperture pinhole, a 2 x 2 mosaic of an order 19 x 19 URA pattern, and an order 38 x 38 random-seeded array. Figure 1 shows the pinhole on the left, URA mask pattern in the center, and an example of a randomly generated mask array on the right.

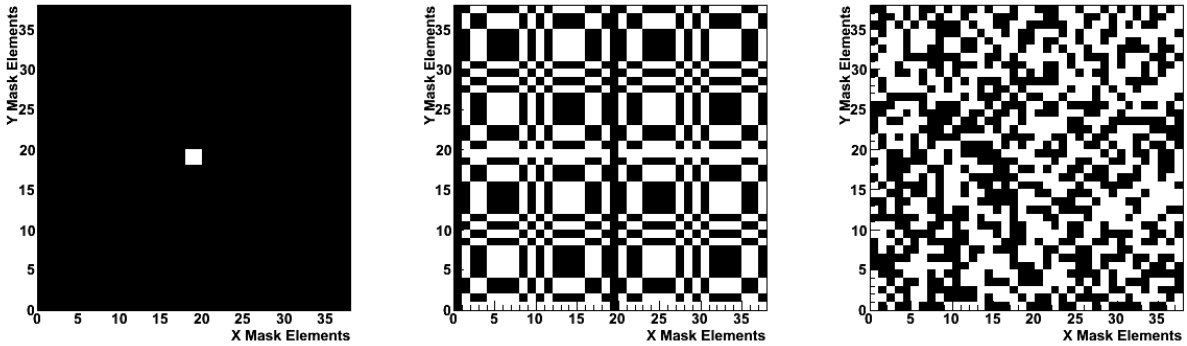

Figure 1 - (From left to right) Example of simulated pinhole, URA, and random mask design for coded aperture imaging.

2.2. Fast neutron coded aperture imager

All simulations of the mask arrays are performed using a model for a fast neutron coded aperture imager developed by Oak Ridge National Laboratories and Sandia National Laboratories [10].

The imaging space was chosen to be a 3 m x 3 m plane at a distance of 6 m in front of the detection plane. This space was divided into 60 bins in the horizontal and vertical directions and a single bin 1cm wide in depth. Within the imaging space, two source distributions are investigated. One scenario consists of a single point source, displaced from the origin, with uniformly distributed background. The second scenario consists of an extended source distribution, also with a uniformly distributed background. This extended source consists of a ring, a point source and a line source. Imaging systems are frequently tested using point sources because they reveal the inherent angular resolution of a detector system, but an extended source was included in this investigation because many real world sources of interest are larger than the angular resolution of the detector system [11]. Figure 2 shows the source distributions in the imaging plane for the point source test case on the left and the extended source test case on the right. For the point source test case, we consider a low signal to background scenario, with 1.3 detected n/s for the source, and 24.6 detected n/s for the background, both integrated over the detector plane. For the extended source test case, the neutron source rate from each of the ring and rectangle was chosen to be approximately equivalent to what we expect from an IAEA significant quantity of weapons grade plutonium ($4x10^5$ n/s). The detected neutron rate was calculated at the given distance, accounting for the mask attenuation and assuming 70%

detection efficiency, yielding ~50 s^{-1} from each extended source for a 50% open fraction. The point source in the multi-source configuration was taken to emit an order of magnitude fewer neutrons. The rate of uniform background for the multi-source configuration was 150 s^{-1}.

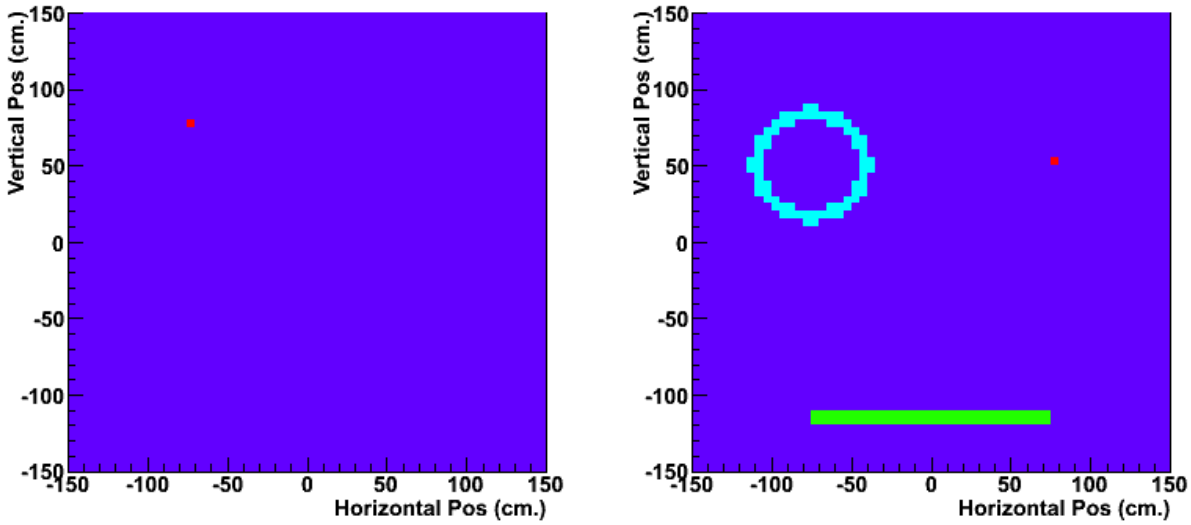

Figure 2 – Simulated soure distributions for point source and extended source (point, ring and line) scenarios.

2.3. Image quality FOM

Many techniques are used to quantify the image quality that results from an image reconstruction obtained using coded aperture. Previous techniques employed include using the signal-to-noise ratio of the reconstructions and using the magnitude of the coding noise as a percentage of the signal peak [2,12]. For this investigation, though, the image quality FOM must be robust enough to handle both a point source and extended source test case. A χ^2 quantity defined as

$$\chi^2 = \frac{2}{I}\sum_{i=1}^{I}\frac{\left(x(i)-\hat{x}(i)\right)^2}{x(i)-\hat{x}(i)}, \qquad \textbf{(1)}$$

where $x(i)$ is the reconstructed image, $\hat{x}(i)$ is the true image, and I is the total number of image pixels, was chosen for this investigation. This is a technique widely employed in medical imaging where very diffuse sources are typically imaged [13]. This quantity allows for the direct comparison of the true and reconstructed image by examining differences pixel by pixel. By evaluating the magnitude of this quantity, it can be determined quantitatively how much the reconstruction diverges from the true image. Note that because this is a χ^2, a lower value indicates an improvement in image quality.

It should also be noted that this FOM is only valid for the case of Monte Carlo simulations where a true source distribution is known and can be used for the pixel-by-pixel comparison. In the case

of image reconstruction from measured data it is clear that the exact true source distribution is not available and would need to be estimated.

Monte Carlo simulations were performed by first generating a detector response function for the mask pattern to be simulated. This was done by estimating the average attenuation through the mask from each source bin in the image space to each detector pixel using a ray tracing algorithm. This attenuation map was normalized to provide a probability density (PD) over the image plane for each source bin. The PD for a source distribution is then the normalized sum of source bin PDs weighted by the appropriate source strength. To model an observation, a number of random events are then generated out of this source distribution PD according to the desired source strength and dwell time.

All reconstructions are performed using an MLEM iterative reconstruction algorithm [7]. The number of iterations used is dependent upon the test case at hand. For the point source test case, 140 iterations was determined to be the optimum to obtain the most statistically sound image reconstruction [14]. For the extended source case, the number of iterations approached 300.

2.4. Optimization methods

2.4.1 General optimization of open fraction

The random mask was first optimized for open fraction by employing a general scheme that involved generating the image quality FOM for a variety of open fractions and observing any trends in the resultant values. This was done by generating random masks with open fractions between 5% and 95% in 5% increments. For each open fraction, 100 different random masks were generated, and a high statistics FOM, designated as Q, was determined as follows. For each of the 100 mask patterns, 50 test datasets were randomly generated—25 using one of the source distributions in Figure 2, and 25 using a 90-degree rotation of the same distribution. An image was reconstructed from each test dataset and the χ^2 comparison to the true distribution was calculated using Eq. (1). The set of 50 χ^2 values was averaged to obtain a value designated as Q^* for each mask pattern. Finally, Q^* values for the 100 mask patterns were averaged to arrive at the value Q for each open fraction. The values of Q are plotted versus open fraction in Figure 6. Curves were generated for both the point source and extended source test case.

In addition to using this scheme for random masks, a Q value was generated for both a URA and pinhole mask. Because each of these mask array types exists for a singular open fraction under the constraints of a specific geometry, only one Q value was generated for each. These values were added to the plot of Q versus open fraction to give a better understanding of the differences in image quality between the different mask types for a specified test case.

2.4.2 Heuristic optimization of mask pattern

For the extended source test case, the random mask was also optimized for open fraction and the mask pattern itself by employing a heuristic optimization algorithm [8]. A hybrid algorithm was

constructed combining elements of SA and the GDA. This is illustrated graphically in Figure 3 and in pseudo-code outlining the algorithm shown below:

Generate an initial random mask configuration, M^0
Choose an initial number of mask pixel flips, F
Choose an initial image quality FOM, Q^0
Choose a convergence speed, S
While (Number of mask pixel flips > 0)
    Make new mask that is M^0 changed by F, M
    Generate Q for M
    If ($Q < Q^0$)
        $Q^0 = Q^0 - S * (Q^0 - Q)$
        $M^0 = M$
    Else
        $F = F - 1$
Stop

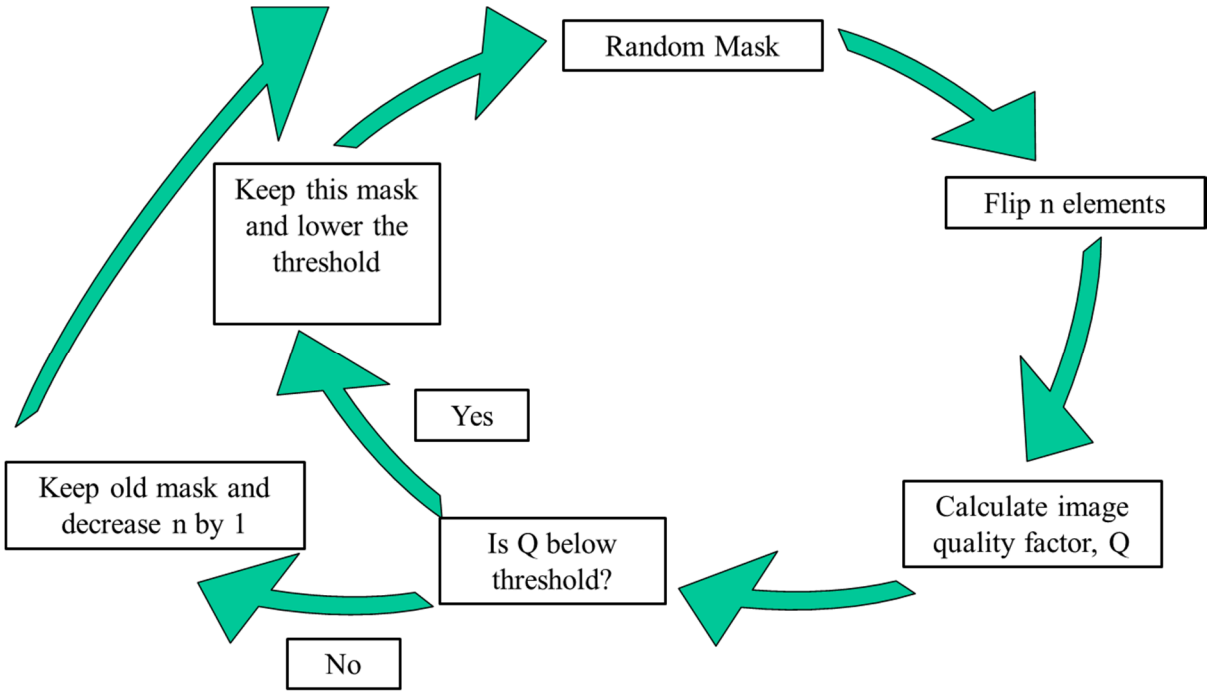

Figure 3 - Illustration of the mask optimization algorithm.

By performing perturbations to the original mask configuration in the form of flipping mask elements from open to close or vice versa and comparing the image quality to Q^0 instead of the image quality of the previous mask, elements of the GDA are incorporated into the algorithm. By gradually changing the number of pixel flips until a stopping condition is met, SA elements are incorporated into the algorithm.

The scheme used to change Q^0 was selected to ensure that Q^0 lowered quickly when the image quality of the current mask is much lower than Q^0 and lowered slowly when only small decreases in the image quality of the current mask occur. As part of this scheme, a convergence speed was selected to allow control over how quickly the optimized mask was selected [2]. If S is selected to be large (~ 0.1 – 1), the answer will converge quickly, but the best answer may not be achieved. If S is much smaller (~ 10^{-5} – 10^{-3}), convergence to the solution is slow but will be closer to ideal. For the simulations performed in this investigation, an intermediate speed of 10^{-2} was used.

3. Results

3.1 Open fraction optimization results

After following the procedures outlined in the previous two sections, the Image Quality Q is plotted as a function of open fraction. Figure 4 shows the Q values for the pinhole, URA, and average random masks at various open fractions using a point source as the test distribution. The red and blue curves indicate the Q values for the URA and pinhole respectively. Error bars on the connected points indicate the one sigma spread on the Q values for the 100 masks simulated at each open fraction.

Figure 5 is the same plot as Figure 4 but with the ring, point, and line test distribution described previously. In both cases it is clear that mask patterns exist that outperform both the pinhole and URA masks. It should also be noted that the optimal open fraction, indicated by the minimum value in the curve of connected points, depends on the test distribution. For the point source distribution, ~45% open produced the best mean Q value and for the extended source distribution, ~30% was best.

Next, in Figure 6 we overlay the Q value vs. open fraction for all of the leading random masks throughout the optimization process for the extended source test distribution. A 50% open mask was used for the starting mask. It can be seen that there is a large clustering around 50% open. This is caused by the optimization algorithm. For a large fraction of the total optimization process a large number of mask elements were being flipped. This caused a lot of fluctuation around the starting conditions, but after some time the algorithm drove the solution toward a minima by decreasing the open fraction. The optimized mask found its way to the optimal open fraction heuristically. The optimized mask pattern has a better Q value than the previously determined 30% open fraction Q value, because that one was averaged over many truly random mask patterns, while this pattern is a result of optimizing for the Q value.

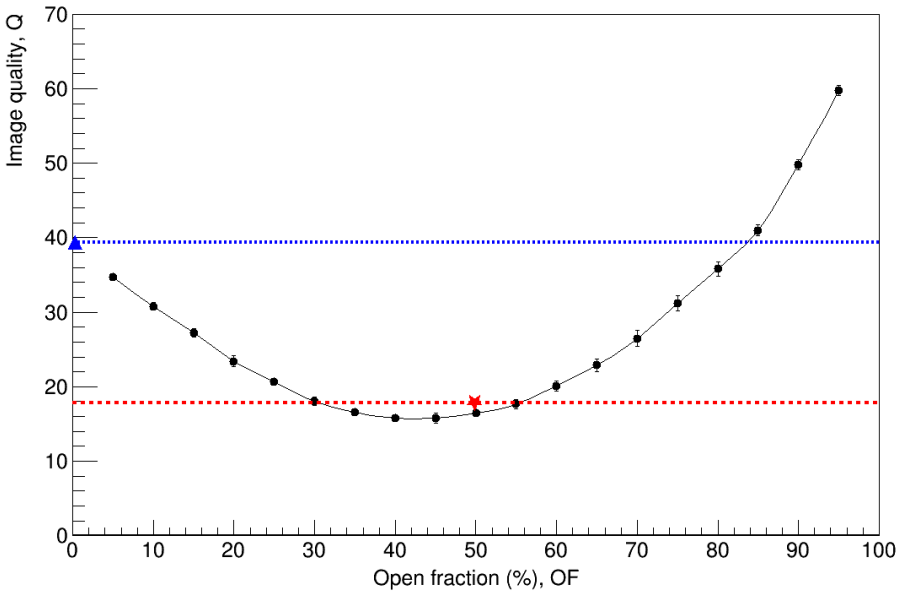

Figure 4 - General optimization of open fraction for point source test scenario. The pinhole Q value is indicated by the blue triangle and blue dotted line, URA Q value by the red star and red dashed line, and the connected points indicated the average Q values for random masks (100 masks per point).

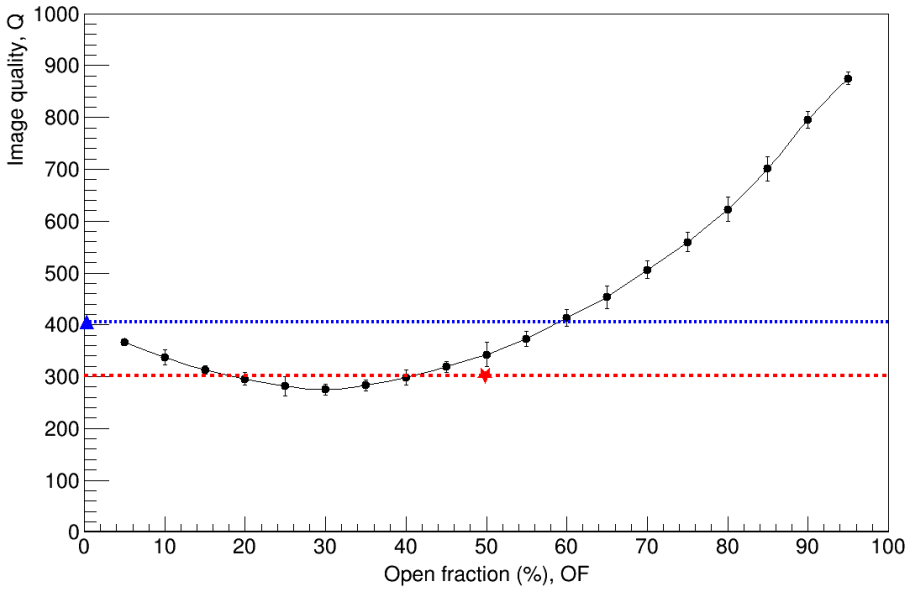

Figure 5 - General optimization of open fraction for extended source test scenario. The pinhole Q value is indicated by the blue triangle and blue dotted line, URA Q value by the red star and red dashed line, and the connected points indicated the average Q values for random masks (100 masks per point).

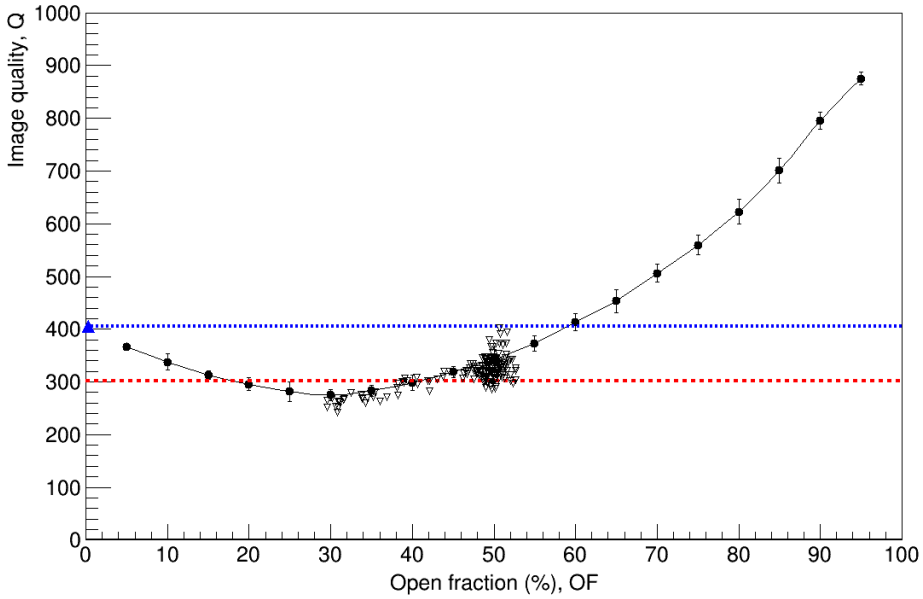

Figure 6 - Heuristic optimization of open fraction for extended source test scenario. The pinhole Q value is indicated by the blue triangle and blue dotted line, URA Q value by the red dashed line, and the connected points indicated the average Q values for random masks (100 masks per point). Each open triangle represents a different random mask pattern.

3.2 Source reconstructions from simulated data

Both the point source and extended source configurations outlined in Figure 2 were reconstructed from the equivalent of 1 hour of simulated data using a pinhole, URA, un-optimized and optimized random mask. Figure 7 shows the reconstructions using a pinhole mask, Figure 8 the reconstructions using a URA mask, Figure 9 the reconstructions using an un-optimized 50% open mask, and Figure 10 the reconstructions using the optimized mask determined from the heuristic optimization algorithm for the extended source scenario. The open fraction of the optimized mask was 30.12%.

For the point source scenario, the pinhole mask reconstructs the correct point source location but with appreciable noise in the rest of the image that could potentially be interpreted as other point sources. Because the URA pattern was tiled (repeated four times to achieve the full mask), the URA mask reconstruction shows symmetrical reconstruction artifacts parallel to the true source position in both the vertical and horizontal directions. Although the un-optimized random mask reconstructs the point source with less background noise and artifacts than its pinhole and URA counterparts, there is still more noise in the background when compared to the optimized random mask. The optimized random mask reconstructs the point source with very minimal background noise and no artifacts.

For the extended source scenario, the pinhole mask reconstructs most the simulated data where the line source is located. Like the point source scenario, there are symmetrical reconstruction artifacts in the extended source reconstruction with the URA mask. There is a symmetric reconstruction of the point, ring and line source. The un-optimized random mask reconstructs each element of the extended source but with enough background noise to eliminate the ability to distinguish the correct location of the point source in this extended source configuration. The optimized random mask shows the point, ring and line source without any substantial ambiguities in the reconstruction.

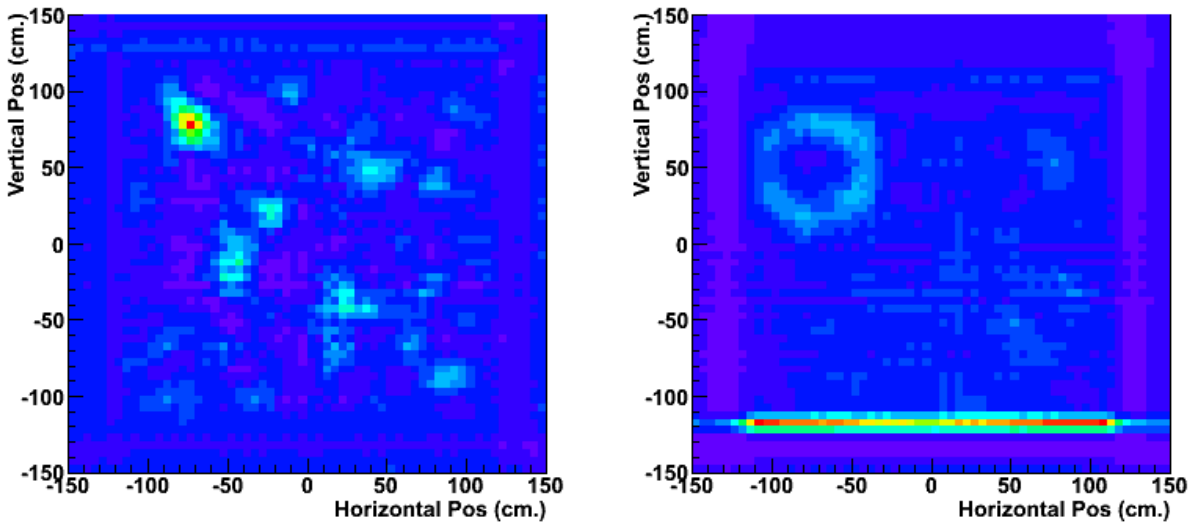

Figure 7 - Simulated reconstruction of point (left) and extended (right) source test cases outlined in Fig. 2 with pinhole mask.

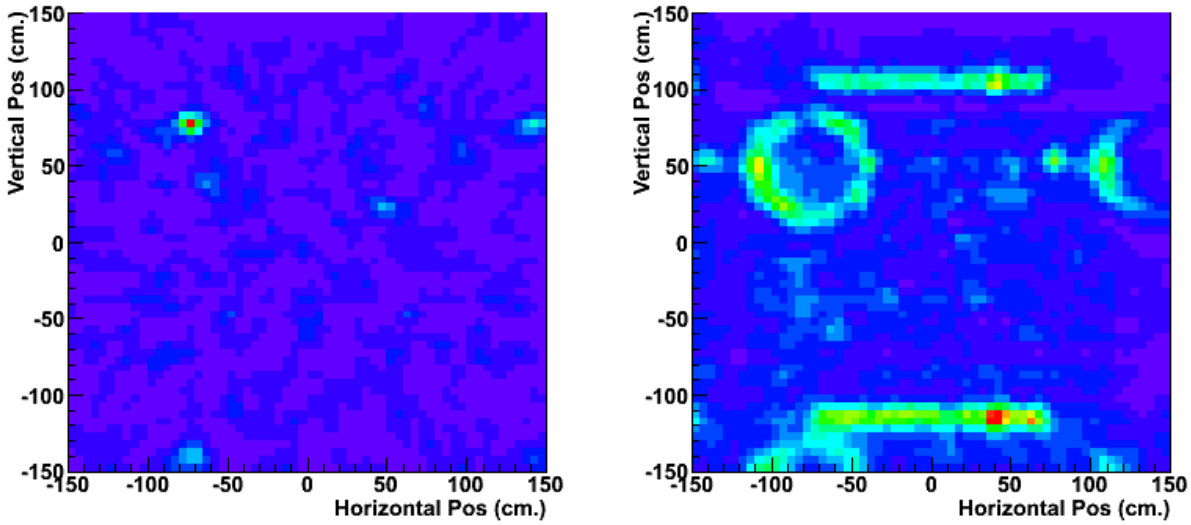

Figure 8 - Simulated reconstruction of point (left) and extended (right) source test cases outlined in Fig. 2 with URA mask.

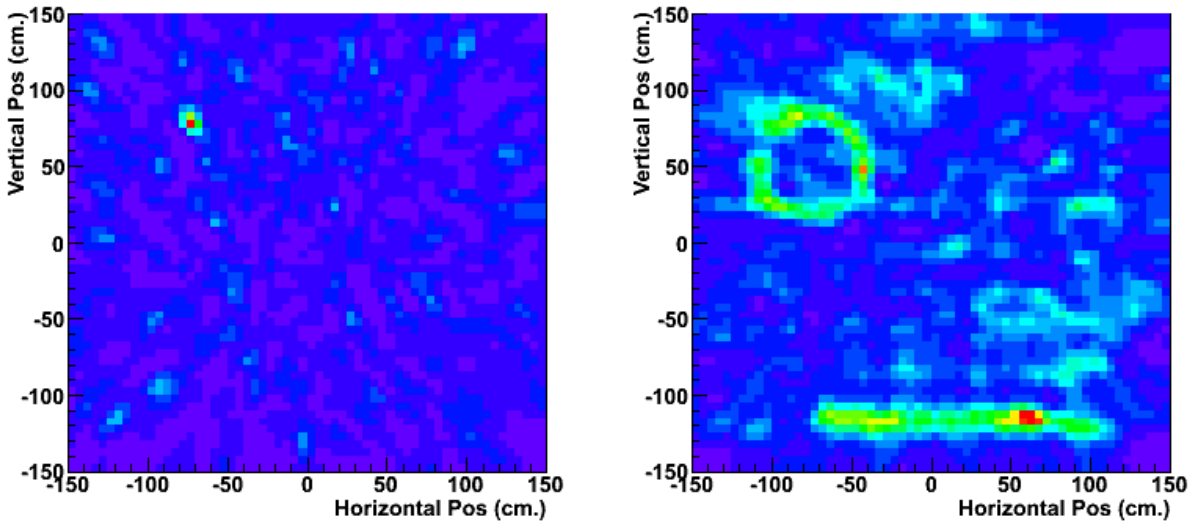

Figure 9 - Simulated reconstruction of point (left) and extended (right) source test cases outlined in Fig. 2 with un-optimized 50% open mask.

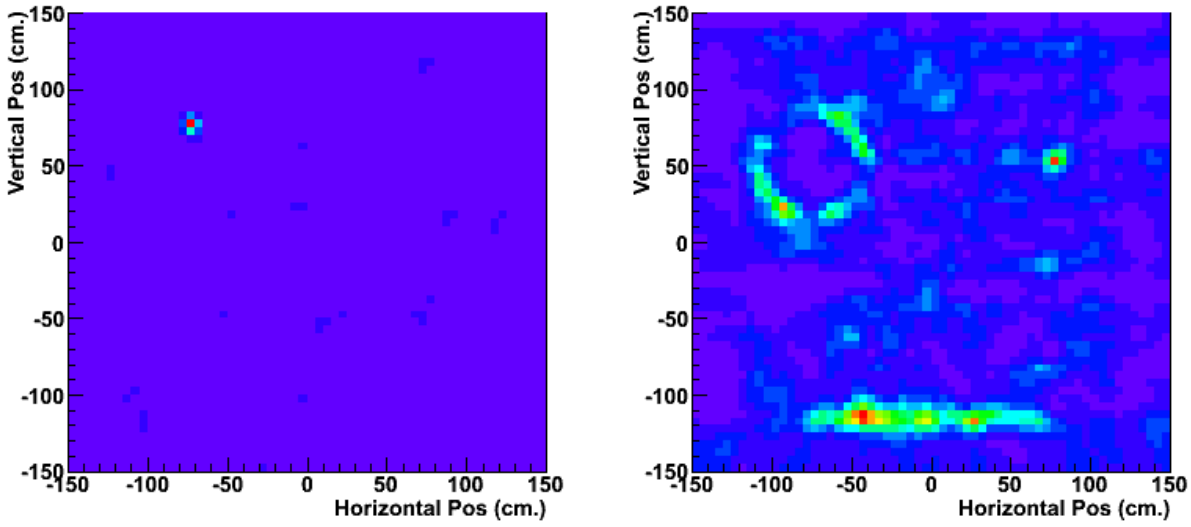

Figure 10 - Simulated reconstruction of point (left) and extended (right) source test cases outlined in Fig. 2 with optimized mask (30.1247% open).

Table 1 outlines a quantitative comparison of the point and extended source reconstructions shown in Figure 7-10. For each mask type investigated, the number of events simulated, which is a function of the open fraction of the mask, and the image quality FOM defined in Equation 1 was tallied.

For the optimized random mask, the calculate image quality FOMs for the point and extended source scenarios match nicely with the respective point and extended source optimization curves shown in Figure 4 and 5 at the open fraction of 30%. Although this mask was optimized for the extended source scenario, the point source reconstruction shown in Figure 10 demonstrates the robustness of this optimized random mask to properly reconstruct source distributions beyond the training set.

	Point Source		Extended Source	
Mask Type	Number of Events ($x10^5$)	Image Quality FOM	Number of Events ($x10^5$)	Image Quality FOM
Pinhole	0.0204	39.8	0.0806	402.25
URA	1.93	17.89	9.10	301.07
Un-optimized Random	1.93	16.51	9.07	341.31
Optimized Random	1.88	17.67	7.64	259.12

Table 1 – Quantitative comparison of point and extended source reconstructions with various mask as shown in Figure 7-10. The optimization was performed separately for each source configuration, so the optimized random masks are different for the point source and extended source columns.

3.3 Source reconstructions from measured data

The optimal mask pattern from the extended source simulations described above was physically constructed and used as the mask for the coded aperture imager in a series of extended source measurements. The mask shown in Figure (left) consists of 1,010 - 1.9cm x 1.9cm x 10.2cm high density polyethylene (HDPE) blocks inserted into an aluminum pegboard using plastic dowels. This was used in place of the standard HDPE URA mask in the existing coded aperture imager (Figure right).

A set of extended sources were designed that produce a signature similar in some ways to the simulated test configuration. This was accomplished by moving a ^{252}Cf fission neutron source through a three dimensional pattern and integrating the measurements throughout the entire movement. In this way, an extended source with the strength of the ^{252}Cf neutron source (~4x10^{5} n/s) is simulated.

The optimized mask was placed one meter in front of the detection plane (center to center). The sources to be imaged were located 2.5 meters from the mask center. Figure top row shows the reconstructed image using one extended source ~40 cm next to a second ^{252}Cf point source with ~1/10th the fission rate. This best represents the test configuration that was used in the optimization, although the line source component of that test configuration was not emulated experimentally.

In all configurations, comparable measurements were taken with the 19x19 tiled URA with 2cm x 2cm x 10cm mask elements. Figure shows the reconstructions for both masks using 1 hour measurements of: one extended source and one point source (top row), two extended sources with a large separation (2nd row), two extended sources close together (3rd row), and a point source through 10cm of lead and 10cm of HDPE (bottom row).

Because the true source distribution is unknown, we cannot use the quantifier, Q, to evaluate these images. However, it can be seen visually that the URA pattern seems to outperform the optimized random pattern for most distributions with the notable exception of that found in the top row. This distribution includes both a point source and an extended source and most resembles the test distribution used to optimize the random mask. Though in all cases, there are more reconstruction artifacts in the background regions of the images, the reconstruction appears to be more accurate in the source regions of this distribution.

There are at least two possible reasons that these artifacts are produced:

1. The pegboard construction of the pseudo-random mask lacked great precision. Each mask element was able to rotate in position and therefore were not necessarily well aligned.
2. The optimization procedure was not defined with enough variation to ensure that source distributions other than those found in the training set would reconstruct well. Better performing and more robust patterns might result if the procedure were to include

transformations other than three 90 degree rotations. For instance, scaling, translation, and arbitrary rotations may produce better results at the cost of longer computation times.

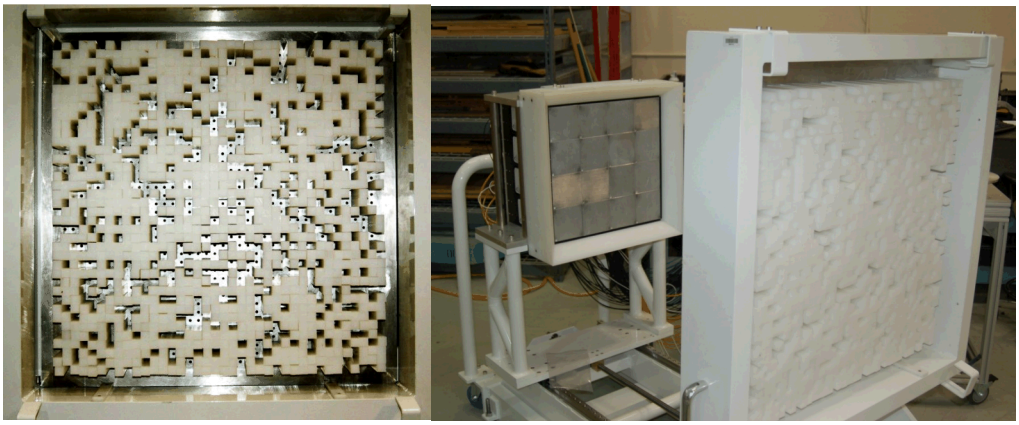

Figure 11 - Photograph of the optimized random mask (left) and the fast neutron coded aperture imager with the optimized random mask installed (right).

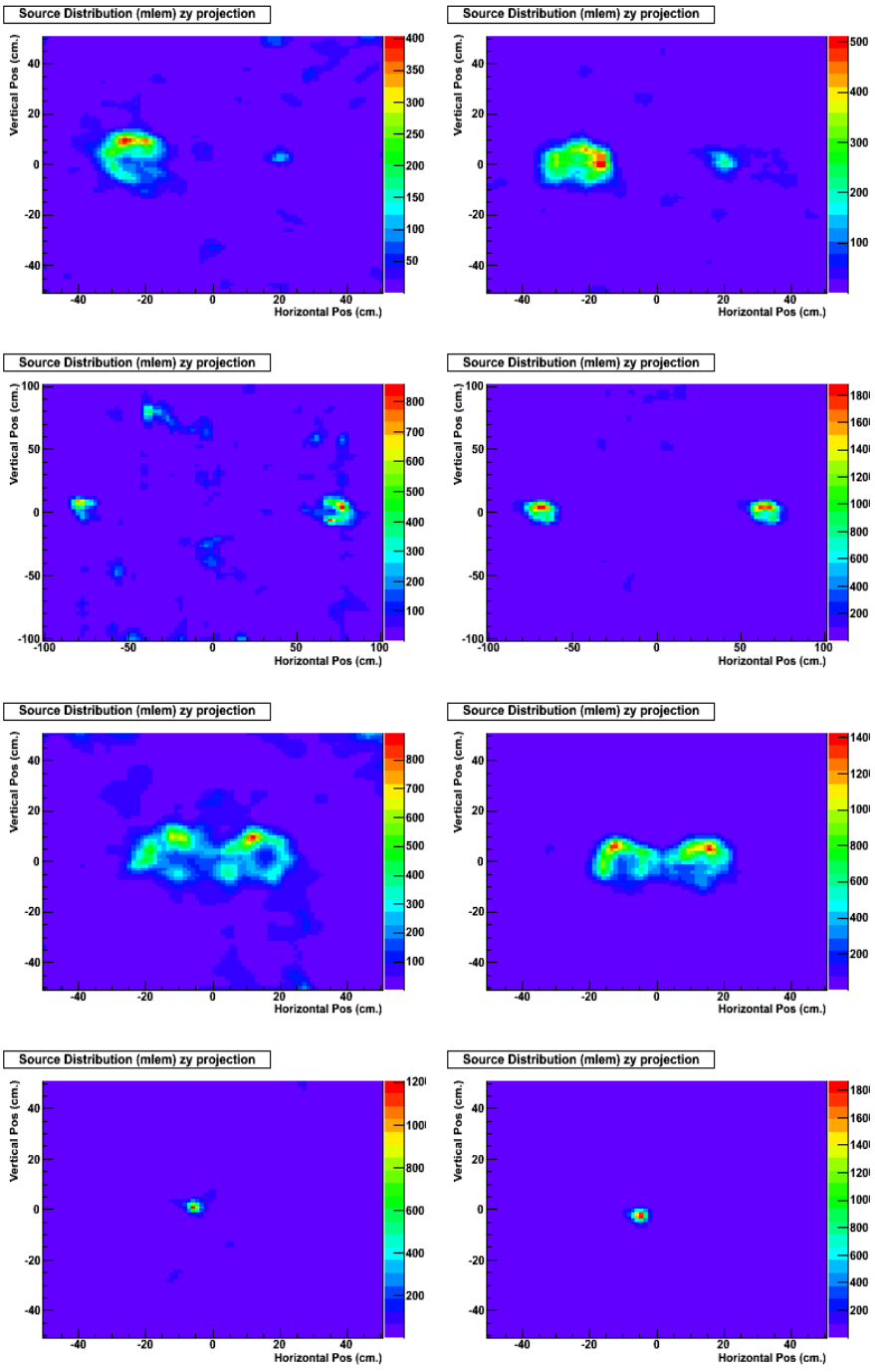

Figure 12 - Reconstruction of various source configurations from measured data for URA (right) and optimized random mask (left).

4. Conclusions

Through a combination of Monte Carlo modeling and image reconstruction algorithms we have demonstrated that it is possible to optimize coded aperture masks to perform at least as well as

URA patterns. An important part of the optimization is that it converges to a mask open fraction that is optimal for a givensource distribution and signal-to-noise ratio.

To test this approach we designed, constructed, and demonstrated an optimized random mask in a fast neutron coded aperture imager. Preliminary results are promising. However, it is likely that our quantification of performance was not robust enough to deal with source distributions that differ too much from the test distributions that were used for optimization. This is made manifest by worse image reconstruction relative to a URA mask pattern for all but the configuration most like the test distribution.

Future work will include improvements to our definition for image quality to better represent the range of source distributions that may be of interest.

Acknowledgments

We thank Paul Hausladen, Matthew Blackston, and Jason Newby at Oak Ridge National Laboratories for leading the development of the neutron coded aperture imager, and for useful discussions related to coded aperture image reconstruction. We thank the NNSA Defense Nuclear Nonproliferation Office of Research and Development for funding this work.

Sandia National Laboratories is a multi-program laboratory managed and operated by Sandia Corporation, a wholly owned subsidiary of Lockheed Martin Corporation, for the U.S. Department of Energy's National Nuclear Security Administration under contract DE-AC04-94AL85000.

References

[1] E. Caroli, *et. al.*, "Coded Aperture Imaging in X- and Gamma-Ray Astronomy," Space Sci. Rev. **45**, 349-403 (1987).

[2] A. Busboom, *et. al.*, "Combinatorial Design of Near-Optimum Masks for Coded Aperture Imaging," Proc. IEEE Int. Conf. Acoust., Speech, Signal Processing **4**, 2817-2820 (1997).

[3] S. R. Gottesman and E. E. Fenimore, "New family of binary arrays for coded aperture imaging," Appl. Optics **28**, 4344-4352 (1989).

[4] E. E. Fenimore, "Coded aperture imaging: predicted performance of uniformly redundant arrays," Appl. Optics **17**, 3562-3570 (1978).

[5] E. E. Fenimore and T. M. Cannon, "Coded aperture imaging with uniformly redundant arrays," Appl. Optics **17**, 337-347 (1978).

[6] R. Accorsi, *et. al.*, "Optimal coded aperture patterns for improved SNR in nuclear medicine imaging," Nucl. Instrum. Methods Phys. Res., Sect. A **474**, 273-284 (2001).

[7] L. A. Shepp and Y. Vardi, "Maximum Likelihood Reconstruction for Emission Tomography," IEEE Trans. Med. Imaging **1**, 113-122 (1982).

[8] A. Busboom, *et. al.*, "Uniformly redundant arrays," Exp. Astron. **8**, 97-123 (1998).

[9] G. Dueck, "New Optimization Heuristics: The Great Deluge Algorithm and the Record-to-Record Travel," J. Comput. Phys. **104**, 86-92 (1993).

[10] P. Marleau, *et. al.*, "High-resolution imaging of fission energy neutrons," Transactions of the Institute of Nuclear Materials Management 53rd Annual Meeting, Orlando, FL, July 15-19 (2012).

[11] J. P. Sullivan, *et. al.*, "Extended radiation source imaging with a prototype Compton imager," Appl. Radiat. Isot. **67**, 617-624 (2009).

[12] G. K. Skinner and J. E. Grindlay, "Coded masks with two spatial scales," Astron. Astrophys. **276**, 673-681 (1993).

[13] A. Gaitanis, *et. al.*, "PET image reconstruction: A stopping rule for the MLEM algorithm based on propertiee of the updating coefficient," Comput. Med. Imaging Graphics **34**, 131-141 (2010).

[14] K. J. Coakley "A Cross-Validation Procedure for Stopping the EM Algorithm and Deconvolution of Neutron Depth Profiling Spectra," IEEE Trans. Nucl. Sci. **38**, 9-15 (1991).